

PHOTONICS Research

Filter-free high-performance single-photon emission from a quantum dot in a Fabry–Perot microcavity

JIawei YANG,^{1,†} ZHIXUAN RAO,^{1,†} CHANGKUN SONG,¹ MUJIE RAO,¹ ZIYANG ZHENG,¹ LUYU LIU,¹ XUEBIN PENG,¹ YING YU,^{1,2,*}  AND SIYUAN YU^{1,2}

¹State Key Laboratory of Optoelectronic Materials and Technologies, School of Electronics and Information Technology, Sun Yat-sen University, Guangzhou 510006, China

²Hefei National Laboratory, Hefei 230088, China

[†]These authors contributed equally to this work.

*Corresponding author: yuying26@mail.sysu.edu.cn

Received 18 March 2024; revised 10 July 2024; accepted 17 July 2024; posted 18 July 2024 (Doc. ID 523970); published 6 September 2024

Combining resonant excitation with Purcell-enhanced single quantum dots (QDs) stands out as a prominent strategy for realizing high-performance solid-state single-photon sources. However, optimizing photon extraction efficiency requires addressing the challenge of effectively separating the excitation laser from the QDs' emission. Traditionally, this involves polarization filtering, limiting the achievable polarization directions and the scalability of polarized photonic states. In this study, we have successfully tackled this challenge by employing spatially orthogonal resonant excitation of QDs, deterministically coupled to monolithic Fabry–Perot microcavities. Leveraging the planar microcavity structure, we have achieved spectral filter-free single-photon resonant fluorescence. The resulting source produces single photons with a high extraction efficiency of 0.87 and an indistinguishability of 0.963(4). © 2024 Chinese Laser Press

<https://doi.org/10.1364/PRJ.523970>

1. INTRODUCTION

Self-assembled quantum dots (QDs) play a crucial role in generating quantum states of light, including single photons [1–3], entangled photon pairs [4–6], and cluster states [7–9]. To fully harness QDs' capabilities, it is essential to control the preparation of low-multi-photon contributed, indistinguishable photons and efficiently extract them from the semiconductor bulk for collection by a free-space lens or optical fiber. The initial hurdle of efficient preparation has been effectively addressed by employing fast pulsed resonant excitation, eliminating dephasing and time jitter, and resulting in near-unity indistinguishable single photons [10]. The subsequent challenge of efficient extraction has been addressed by embedding QDs in Purcell-enhanced photonic cavities like micropillars [11], open cavities [12], circular Bragg gratings [13], and photonic crystal waveguides [14]. The combination of these two strategies produces pure and indistinguishable photons with high extraction efficiency [15–19].

However, a critical obstacle to achieving high end-to-end efficiency lies in preventing the excitation laser pulse from entering the collection path. Typically, separating the pump laser from the signal using pump-probe cross-polarization results in at most a 50% signal reduction with isotropic cavities [10,17].

Recent advancements have alleviated this issue by developing anisotropic cavities, induced by geometry ellipticity [18] or material birefringence [16,20]. In this approach, a circularly polarized quantum emitter is brought into resonance with one of the linearly polarized cavity modes for efficient polarized photon extraction, while the perpendicular one is used for laser exclusion. The state-of-the-art QD-based single-photon source in an open microcavity has achieved high end-to-end efficiency (>71.2%) and high photon indistinguishability (>98.5%) [20]. However, optimizing the pulse width remains crucial to balance excitation efficiency [20] and the risk of QD re-excitation [21]. Meanwhile, polarized cavities' limitation on variable polarization of single photons hinders the scalability of complex photonic states like cluster states [7].

A straightforward approach to overcome this limitation is resonant excitation of the emitter via non-cavity modes perpendicular to the collection axis, a method used for QDs embedded in planar cavities [22] and waveguides [23,24]. Despite its attractiveness, implementing this method in high-Purcell-enhanced vertical cavities remains challenging due to the isolated structure of micropillars [25,26]. Huber *et al.* attempted to integrate connected waveguides with micropillars; however, it resulted in fundamental mode leakage and laser scattering at the micropillar-waveguide interface, achieving only a Purcell factor

of 2.5 [27]. For open cavities, introducing excitation at another axis on top of the existing two 3D independent adjustments of mirrors is challenging. Here, we propose a feasible solution by introducing a novel design that features a micrometer-scale parabolic lensed-defect between two distributed Bragg reflectors (DBRs). This Gaussian-shaped defect in a Fabry–Perot cavity was initially conceptualized in 2013 [28] and later implemented in QD systems [29,30]. Thanks to its planar microcavity design, it suppresses unwanted pump lasers and achieves filter-free Rabi oscillations with an optimal autocorrelation value of $g^{(2)}(0) = 0.0322(2)$, indicating no spectral or polarization filters are used. Moreover, combining resonant excitation with the Purcell effect enables the generation of single photons with a simultaneous high extraction efficiency of 0.87 and indistinguishability of 0.963(4).

2. RESULTS

A. Design Concept

To achieve resonant excitation and effectively discriminate the QD signal from stray laser light, we implemented an orthogonal excitation/detection geometry [Fig. 1(a)]. A single-mode fiber, positioned on a three-axis displacement stage, is placed within a few micrometers of the cleaved sample edge. A tunable, mode-locked Ti:Sa pulsed laser, polarized in-plane, is introduced through the fiber to excite the QDs embedded in a 2λ monolithic microcavity. This microcavity features a parabolic lensed-defect within a Fabry–Perot distributed Bragg reflector (DBR) cavity. Lateral confinement is provided by the parabolic lensed-defect in the central spacer layer, as shown in the cross-section scanning electron microscope (SEM) image in Fig. 1(b). This design results in vertically emitted photons that are collected by an objective and directly coupled into a single-mode fiber without the need for spectral or polarization

filtering. The spatial overlap of the QD emission with the cavity mode is achieved through well-established deterministic positioning techniques [31]. Detailed fabrication processes are provided in Appendix A and our previous report [30]. Theoretically, an extraction efficiency of up to 94.9% and a Purcell factor of 40 are achievable [30].

In experiments, the laser, directed onto the cleaved side facet of the sample, effectively couples into the planar waveguide mode, enabling low-loss transmission [Figs. 1(c) and 1(d)]. Notably, our methodology enables QD excitation at a distance greater than 400 μm from the cleaved edge of the sample. The orthogonal alignment of the resonant excitation laser's propagation and the QD emissions minimizes upward scattering, eliminating the need for polarization filtering. Importantly, our approach is more versatile than cross-polarization excitation, allowing the QD emission to have any desired polarization for applications like BB84 [32] or specific polarizations for other applications such as boson sampling [33].

B. Purcell-Enhanced Single-Photon Emission under Spatially Orthogonal Excitation

To demonstrate our approach, we apply spatially orthogonal resonant excitation to a single-QD-charged exciton (CX) that is deterministically coupled to microcavities with distinct circular and linear polarizations. Figures 2(a) and 2(b) display the photoluminescence (PL) spectra of our microcavity modes under high-power above-band excitation, exhibiting splits into horizontally and vertically polarized (H- and V-polarized) modes at 11.05 GHz and 86.50 GHz in Cavities A and B, respectively. The observed mode splitting is primarily attributed to the residual asymmetric uniaxial strain in the semiconductor material and minor structural asymmetries induced by the dielectric top DBRs, consistent with phenomena observed in open cavities [16,20]. Further adjusting the magnitude of

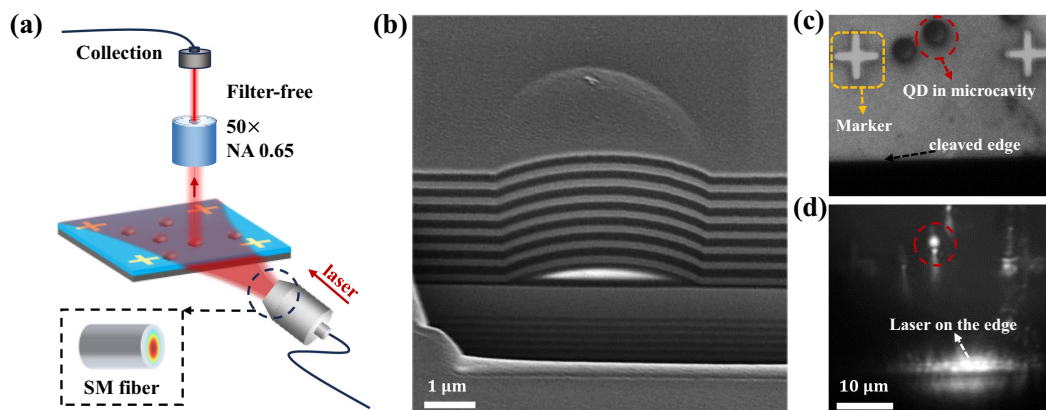


Fig. 1. Scheme of spatially orthogonal excitation. (a) Schematic of the spatially orthogonal excitation setup, showing the alignment of a single-mode optical fiber and the sample inside a cryostat. The optical fiber, actuated by a displacement stage with a custom mold and metal tape, is placed a few micrometers from the sample's cleaved edge. Signal light, collected by an objective with a numerical aperture (NA) of 0.65, is directed perpendicular to the incident laser direction and coupled into a single-mode fiber. (b) A scanning electron microscope (SEM) image of the sample, consisting of seven pairs of $\text{SiO}_2/\text{TiO}_2$ top DBRs and 46 pairs of $\text{GaAs}/\text{Al}_{0.95}\text{Ga}_{0.05}\text{As}$ bottom DBRs. Quantum dots (QDs) are located within a parabolic microcavity at the center. (c) A frontal EMCCD image of the sample showing the cleaved edge, microcavity with QD, and reference marker. (d) A frontal EMCCD image capturing the spatially orthogonal excitation of QDs. The incident laser, with specific polarization, couples into the sample, enabling long-distance, low-loss propagation via waveguide modes and exciting QDs along the path. Note that markers and other cavities in the sample could cause some scattered light. However, if the scattered light is sufficiently distant from the microcavity under investigation, its impact on the measurements is minimal and can be considered negligible.

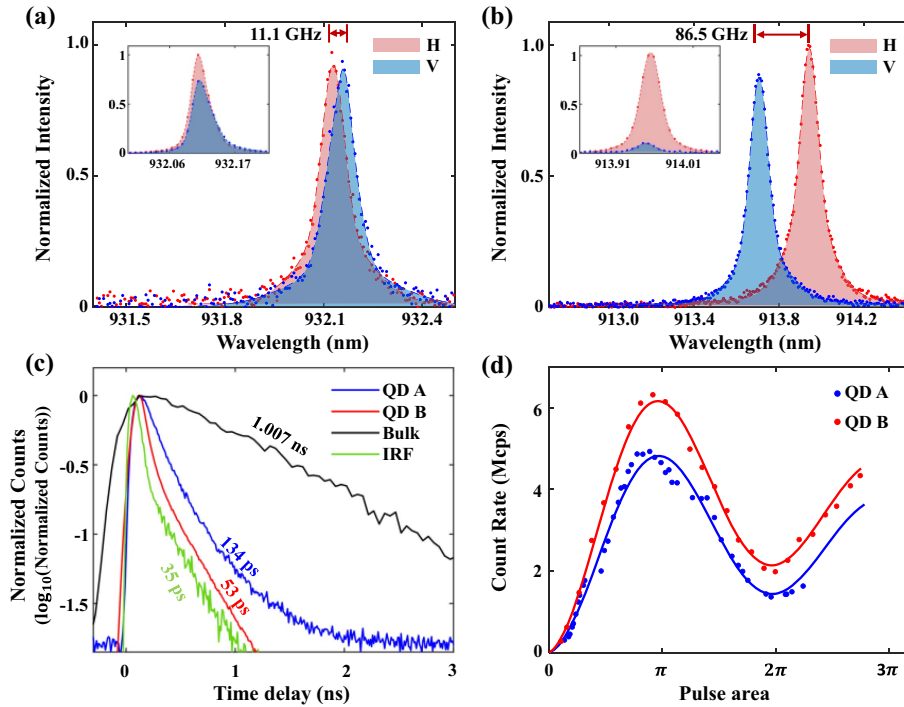


Fig. 2. Spatially orthogonal resonant single-photon characterization of a QD in microcavity. (a) Photoluminescence (PL) spectra of Cavity A with a small splitting $\Delta\omega = 11.05$ GHz. The H-polarized mode (highlighted in red) is at 932.125 nm with a linewidth of 0.098 nm ($\delta\omega_H = 33.84$ GHz), while the V-polarized mode (highlighted in blue) is at 932.157 nm with a linewidth of 0.102 nm ($\delta\omega_V = 35.22$ GHz). The inset shows that the H-polarized contribution of the QD is 57.80% while the V-polarized mode is 42.2%. (b) Cavity B exhibits a larger split of $\Delta\omega = 86.50$ GHz. The H-polarized mode is at 913.945 nm with a linewidth of 0.111 nm ($\delta\omega_H = 39.84$ GHz), and the V-polarized mode is at 913.704 nm with a linewidth of 0.108 nm ($\delta\omega_V = 38.78$ GHz). The inset shows the highly polarized single photon, with 91% of QD's emission in the H-mode. (c) Lifetime of resonant fluorescence of QD in microcavity under spatially orthogonal excitation. Under the “ π pulse” condition, we extracted an ultra-short lifetime from the typical lifetime histogram of CX, which is ~ 134 ps (blue curve) for QD A in Cavity A and ~ 53 ps (red curve) for QD B in Cavity B. With the lifetime of ~ 1.007 ns (black curve) in the bulk material, we obtain the Purcell factor of ~ 7.5 in Cavity A and ~ 19 in Cavity B. The instrument response function (IRF) is illustrated by the green line, with a τ of 35 ps. (d) The relationship between the pump strength and the count rate of the avalanche photon detector (APD), revealing a full Rabi oscillation curve. The curves represent the numerical fitting results, with the maximum count rates of QD A and QD B being ~ 4.93 Mcps and ~ 6.23 Mcps, respectively. The “ π pulse” of QD in Cavity A and Cavity B corresponds to a power of 66 μ W and 36 μ W, respectively.

mode-splitting can be achieved by applying strains on the GaAs substrate [34]. The linewidths of the H mode in Cavity A and Cavity B are 0.098 nm and 0.111 nm, corresponding to measured quality factors of 9511 and 8234, respectively. In a bi-refracting cavity, the spontaneous radiation rate of the exciton's circularly polarized transition is expected to redistribute into H and V polarizations [18]. Resonance of the QD with the cavity H mode, achieved through minor temperature adjustments, yields predicted polarized spontaneous emission ratios ζ_H of 0.578 in Cavity A and 0.910 in Cavity B [see insets of Figs. 2(a) and 2(b)].

In the pursuit of creating a highly bright and indistinguishable single-photon source, we conducted pulsed resonance fluorescence for the CX under laser excitation with an 80.1 MHz repetition rate. Time-resolved resonance fluorescence measurements reveal shortened radiative lifetimes for the QDs on resonance with cavities to $\tau_{\text{on}} \sim 134$ ps [Cavity A, blue line in Fig. 2(c)] and ~ 53 ps [Cavity B, red line in Fig. 2(c)]. Compared with the average lifetime for the QDs in bulk from the same area [black line in Fig. 2(c)], a Purcell factor F_p of ~ 7.5 (19) is achieved in Cavity A (B).

Figure 2(d) presents the detected single-photon flux as a function of driving laser strength, showing a complete Rabi oscillation curve for both microcavities, indicative of coherent two-level system control. Notably, this marks the first observation of pulsed resonance fluorescence for QD-in-microcavity systems under spatially orthogonal excitation, achieved without employing any spectral filter. Under the “ π pulse” condition, the avalanche photon detector (APD) records approximately 4.93 Mcps in Cavity A and 6.23 Mcps in Cavity B. Accounting for the setup efficiency and the APD correction factor, an extraction efficiency of 0.63 is obtained for Cavity A and 0.87 for Cavity B. A comprehensive calibration of the system efficiency is detailed in Appendix C. For both circularly and linearly polarized microcavities, spatially orthogonal excitation proves to be an excellent scheme for resonant fluorescence experiments.

C. Comparison of Spatially/Polarized-Orthogonal Excitation

We then assess the single-photon characteristics in Cavity B using both spatially orthogonal and polarized-orthogonal

excitation strategies [Figs. 3(a) and 3(b)]. In polarized-orthogonal excitation, the QD is excited by a V-polarized laser, and H-polarized single photons are collected. As depicted in Fig. 3(b), only about 4.64×10^6 photons per second are detected at π pulse. We estimate that the probability of emission into the H-polarized mode, denoted as β_H , can be determined to be $\beta_H = [F_p / (F_p + 1)] \times \zeta_H$, revealing a value of 0.865 in Cavity B.

To characterize the second-order coherence of the single-photon source, we use a Hanbury Brown and Twiss setup under conditions of $I = 0.6 \cdot I_{\text{Sat}}$ by decreasing the excitation power, where I_{Sat} represents the intensity of resonant fluorescence at the “ π pulse”. The second-order autocorrelation in Fig. 3(c) reveals filter-free $g^{(2)}(0)$ values of 0.0472(2) for spatially orthogonal excitation and 0.0889(7) for polarized-orthogonal excitation, indicating distinct photon antibunching in both cases. Additionally, single-photon coherence is assessed

using a Hong–Ou–Mandel (HOM) interferometer, which measures a 12.48 ns time separation between consecutive single-photon emissions, aligning with the laser pulse timing. The photon correlation histograms in Fig. 3(d) for orthogonal and parallel polarizations show raw HOM visibilities of 0.845(2) for spatially orthogonal and 0.731(4) for polarized-orthogonal excitation. Considering imperfect single-photon second-order coherence and an unbalanced beam splitting ratio in the optical setup, we calculate corrected photon indistinguishabilities of 0.966(2) for spatially orthogonal and 0.899(4) for polarized-orthogonal excitation (see Appendix B). This highlights the high coherence of single photons generated using spatially orthogonal excitation in the microcavity which may be attributed to the QDs’ distinct dipole orientations relative to the excitation and collection pathways.

We investigate the origin of the non-vanishing peak at zero-time delay in the QD-in-microcavity system under spatially

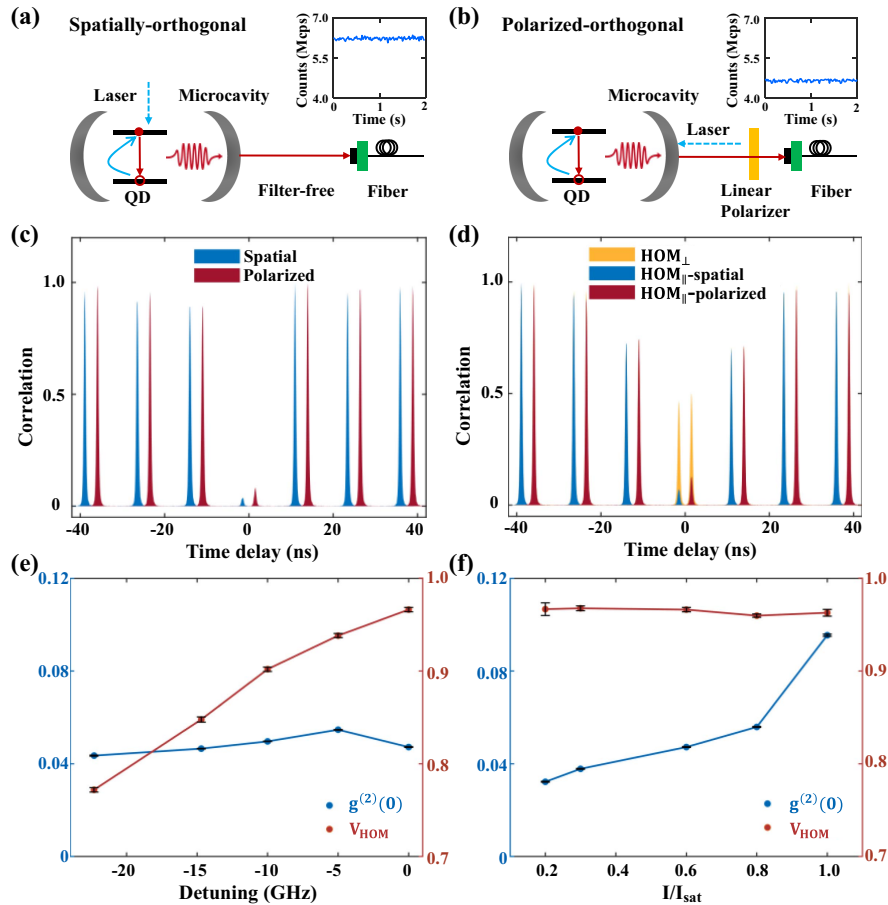


Fig. 3. High-performance single photon in microcavity with different excitation strategies. (a) Schematic of spatially orthogonal excitation, achieving filter-free excitation with a saturated count rate of resonant fluorescence at 6.23 Mcps. (b) Schematic of polarized-orthogonal excitation, where orthogonal polarization filtering reduces the saturation count rate to 4.64 Mcps. (c) Measurement of single-photon second-order coherence, with filter-free excitation yielding a second-order coherence of $g^{(2)}(0) = 0.0472(2)$, and polarized-orthogonal excitation resulting in 0.0889(7). (d) Measurement of HOM interference. A clear contrast at zero-time delay of two orthogonal polarizations is observed, with values of $g_{\parallel}^{(2)}(0) = 0.0822(2)$ and $g_{\perp}^{(2)}(0) = 0.5312(12)$, resulting in an indistinguishability of $V_{\text{raw}} = 0.845(2)$ for spatially orthogonal excitation. For polarized-orthogonal excitation, we attained values of $g_{\parallel}^{(2)}(0) = 0.1518(3)$ and $g_{\perp}^{(2)}(0) = 0.5641(20)$, indicating $V_{\text{raw}} = 0.731(4)$. (e) Temperature dependence of the $g^{(2)}(0)$ (blue) and indistinguishability (red). As the temperature increases, the detuning between the QD and the cavity gradually increases, while $g^{(2)}(0)$ remains stable around 0.952, and indistinguishability decreases gradually. (f) Power dependence of $g^{(2)}(0)$ (blue) and indistinguishability (red). $g^{(2)}(0)$ increases with decreasing power, reaching a minimum of 0.0322(2), influenced by the scattered light while indistinguishability remains stable.

orthogonal excitation, as shown in Fig. 3(e). The $g^{(2)}(0)$ and HOM visibility (V_{HOM}) values vary with sample temperature. Through slightly increasing the temperature, the wavelength of the QD red shifts while the microcavity remains stable. Tuning the QD away from the cavity resonance leads to increased (decreased) lifetime (F_p and V_{HOM}), indicating that microcavities with high Purcell factors are instrumental in mitigating dephasing. However, the value of $g^{(2)}(0)$ remains at ~ 0.048 , which we attributed to a slight amount of laser light scattering into the detection channel. This is further supported by the power-dependent behavior of $g^{(2)}(0)$ and HOM visibility in Fig. 3(f), where $g^{(2)}(0)$ increases with higher laser power while HOM visibility remains almost constant. The best autocorrelation value of $g^{(2)}(0)$ is 0.0322(2) at $I = 0.2 \cdot I_{\text{Sat}}$. As shown in Fig. 1(d), the markers on the sample surface and the protruding microcavity cause scattered light, thereby reducing the single-photon second-order coherence. The resulting single-photon source exhibits a simultaneous high extraction efficiency of 0.87, and indistinguishability of 0.963(4) at the condition of “ π pulse”.

D. Mollow Triplet in the QD-in-Microcavity System under Continuous-Wave Spatially Orthogonal Excitation

The planar cavity structure allows the laser used for resonant excitation to effectively couple with the in-plane guided waveguide mode, simultaneously suppressing background scattering. We transition to continuous-wave resonance excitation

to observe the Mollow triplet, which is a distinctive feature of resonance fluorescence in a strongly driven and dressed two-level system. Figure 4(a) shows a comprehensive power-dependent PL series from the QD, revealing the emergence of two symmetrically spaced sidebands around the central peak with increasing power. In Fig. 4(b), the extracted Rabi splitting is plotted against the square root of the laser power, confirming the theoretically expected linear relationship and demonstrating a significant Rabi splitting of up to 21.4 GHz. Figure 4(c) demonstrates the linewidth of the Rabi sidebands, exhibiting a clear linear dependence on the squared Rabi frequency. These linear trends strongly suggest phonon-dressed QD Mollow triplet emission within the cavity-quantum electrodynamics (cQED) regime in our sample [35].

3. DISCUSSION AND CONCLUSION

In summary, our study introduces a spectral filter-free single-photon source by combining spatially orthogonal resonant excitation with Purcell-enhanced single QDs in a monolithic Fabry–Perot microcavity. This approach effectively separates the excitation laser from the QD emission, eliminating the need for polarization filters and enabling flexible control over the QD’s polarization. These features collectively establish the high-performance attributes of our single-photon source, with an extraction efficiency of 87% and an indistinguishability of 96.3%. The observation of a Mollow triplet with a 21.4 GHz Rabi splitting confirms the presence of a strongly driven and

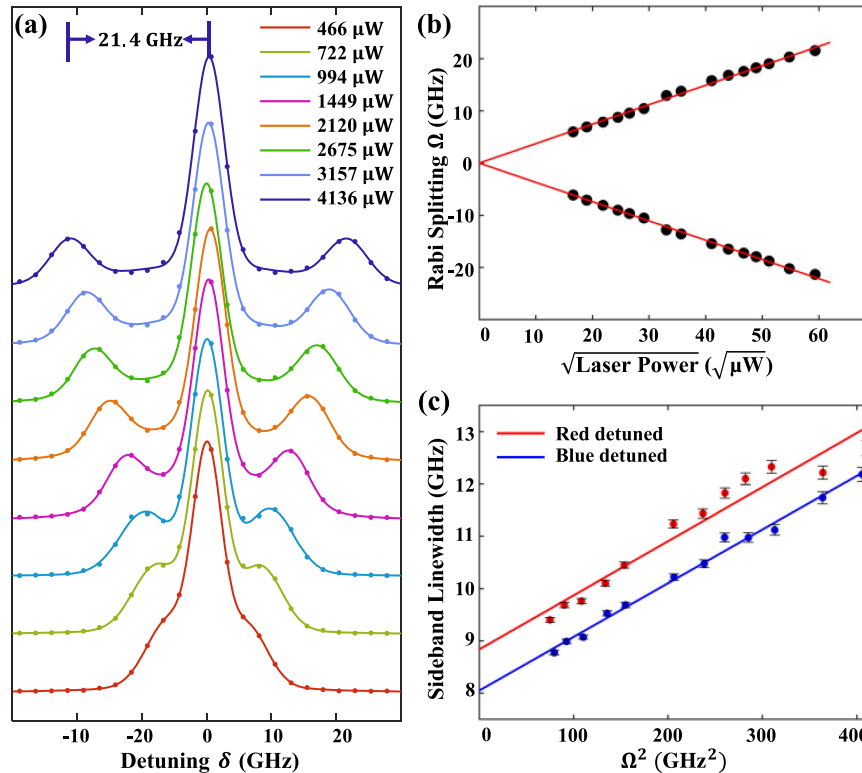


Fig. 4. Mollow triplet of QD in microcavity under spatially orthogonal excitation. (a) High-resolution PL spectra of the QD in a microcavity under spatially orthogonal excitation, showing a maximum Rabi splitting of 21.4 GHz at 4.1 mW laser power. (b) Linear correlation between the Rabi splitting and the square root of laser power. (c) Linear relationship between the linewidths of the side peaks and the square of the Rabi frequency.

dressed two-level system in our microcavity. To further alleviate residual laser scattering under spatially orthogonal excitation, a surface gold coating is proposed to act as a reflective barrier, reducing laser escape through the surface. Additionally, a thicker cavity or a waveguide-cavity scheme [Fig. 7(a)] could enhance waveguide-fiber coupling efficiency and mitigate beam divergence and edge scattering, thus preserving photon purity. This scheme supports a low-loss waveguide mode [Fig. 7(b)], enabling QD excitation away from the edge and facilitating on-chip pumping. Our work provides a foundation for developing efficient, versatile, and miniaturized quantum light sources, which are easily integrable with fiber optics through direct facet attachment [36] or with photonic integrated circuits via grating coupling [37].

APPENDIX A: DEVICE FABRICATION

As shown in Fig. 5, we integrated QDs into a Fabry–Perot microcavity, introducing lateral confinement by incorporating a parabolic lensed-defect between two distributed Bragg reflectors (DBRs), which provided a small mode volume. This design enables a bright single-photon source with a high Purcell factor, producing polarized photons with good suppression of higher-order photon events and high indistinguishability.

Crucial for cavity performance, the DBR's surface reflectivity is determined by the interference of light, depending on the refractive index and thickness of the materials. In our sample, a dielectric DBR of $\text{SiO}_2/\text{TiO}_2$ as the top layer achieves over 0.995 reflectivity with seven pairs, while a GaAs/ $\text{Al}_{0.95}\text{Ga}_{0.05}\text{As}$ semiconductor DBR needs more than 15 pairs for equivalent reflectivity. We used a seven-pair dielectric layer for the top DBR to maintain good curvature even at a few micrometers' thickness, considering the elliptical cavity shape resulting from the flattening of the epitaxial layer when using GaAs materials.

The cavity mode's desired wavelength is obtained by selecting appropriate geometrical parameters of the defect cavity. With the microlens's bottom diameter (B) set to $4\ \mu\text{m}$, the intermediate SiO_2 layer's thickness (S) to 480 nm, and the SiO_2 microlens's height (H) to 350 nm, we simulated the structure with three-dimensional FDTD. The simulation results in

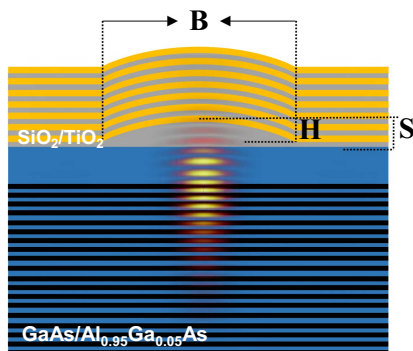


Fig. 5. Cross-section of Fabry–Perot microcavity. Cross-sectional view of the Fabry–Perot microcavity, featuring 46-pair GaAs/ $\text{Al}_{0.95}\text{Ga}_{0.05}\text{As}$ bottom DBRs and seven-pair dielectric top DBRs.

a fundamental mode wavelength of 920 nm, a quality factor exceeding 15,000, a single-photon extraction efficiency of about 0.95, and a Purcell factor (F_p) of approximately 40.

We grew a semiconductor heterostructure on a GaAs (100) substrate using molecular beam epitaxy, incorporating a 500 nm $\text{Al}_{0.8}\text{Ga}_{0.2}\text{As}$ sacrificial layer and 46 pairs of GaAs/ $\text{Al}_{0.95}\text{Ga}_{0.05}\text{As}$ DBRs, with low-density InAs/GaAs QDs at the center of a $2\text{-}\lambda$ GaAs film. The QDs were deposited using an indium flux rate of 0.004 mL/s and an arsenic flux pressure of 5×10^{-7} Torr, capped with 0.5 nm $\text{Al}_{0.2}\text{Ga}_{0.8}\text{As}$ and 6 nm GaAs, followed by an indium flushing technique [38]. We maintained an Al composition of approximately 0.95 in AlGaAs to avoid oxidation challenges. High-precision optical positioning placed QDs at the center of the FP microcavities, followed by fabricating a paraboloid SiO_2 defect using electron beam lithography (EBL) and inductively coupled plasma etching (ICP-RIE). The microcavity was completed with a $\text{SiO}_2/\text{TiO}_2$ top DBR via electron beam evaporation [Fig. 1(b)]. Further fabrication details are provided in our previous report [30].

APPENDIX B: OPTICAL SETUP AND SINGLE-PHOTON PERFORMANCE ESTIMATION

1. Resonance Fluorescence Setup

Figure 6 illustrates our experimental setup for both spatially orthogonal and polarized-orthogonal resonance excitations, as detailed in Fig. 6(a). The spatially orthogonal configuration simplifies the detection path and eliminates the need for a polarizing beam splitter (PBS), thereby reducing system losses and enhancing photon extraction efficiency.

In the spatially orthogonal excitation, we precisely position an optical fiber adjacent to the sample stage using metallic tape. Fine adjustments to the fiber position allow for precise control of the laser's incident angle, ensuring minimal distance to the sample edge to reduce scattered light and maximize coupling efficiency. The laser, incident on the cleaved side facet of the sample [refer to Fig. 1(c) in the main text], couples with the waveguide mode and propagates laterally to excite the quantum dots (QDs) along its path. The orthogonal propagation of the excitation laser and the signal light effectively filters out the laser light.

For polarized-orthogonal excitation, a linear polarizer (LP) is used to match the input beam's polarization to that of the PBS. A half-wave plate selects the output state, aligning with the microcavity's principal V-axis. H-polarized light traverses the PBS and is directed into a single-mode optical fiber. An additional quarter-wave plate in the beam path optimizes the suppression of V-polarized laser light. Residual laser light is filtered out using a long pass filter. A 785 nm continuous-wave laser weakly illuminates the QD to stabilize its charge state. This stabilization is crucial for enabling resonant fluorescence at lower pulse powers for eliminating the laser light. Conversely, in the spatially orthogonal excitation configuration, the incident laser spot is significantly larger, and the power density is sufficiently high to effectively stabilize the charge environment of the QD. The larger spot size and higher power provide a more robust stabilization, reducing the need for an additional off-resonant laser.

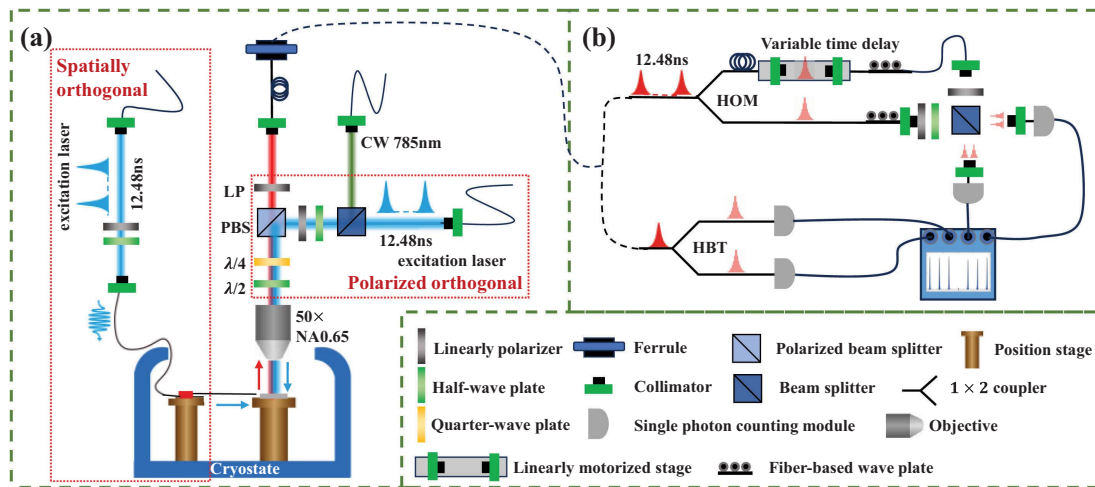


Fig. 6. Experiment setup. (a) Schematic of the spatially orthogonal and polarized-orthogonal excitation setups. (b) Schematic of the Hanbury Brown and Twiss (HBT) setup for measuring second-order coherence and the Hong-Ou-Mandel (HOM) setup for assessing indistinguishability.

The spectral resolution of our system, equipped with the HRS-750 spectrometer from Princeton Instruments featuring a 1800 g/mm blazed grating, is approximately 0.013 nm, which corresponds to ~ 4.7 GHz at 914 nm.

2. Single-Photon Performance Detection and Estimation

Second-order coherence assessment. The experimental arrangement for second-order coherence evaluation is shown in Fig. 6(b). We utilized an 80.1 MHz picosecond pulsed laser for excitation, with the emitted photons being collected via optical fibers and directed to an avalanche photodiode (APD). The detected single-photon signals were fed into a Hanbury Brown and Twiss (HBT) interferometer to measure the second-order correlation function, $g^{(2)}(0)$, from which the coherence properties of the single-photon source are deduced.

Indistinguishability assessment. In the two-photon interference experiment, photons were collected by a single-mode fiber and directed to a Hong-Ou-Mandel (HOM) interferometer equipped with a cube beam splitter ($R:T = 52:48$). A relative delay of 12.48 ns was implemented between the interferometer arms using optical fiber delays and a linearly motorized stage. A half-wave plate was inserted to align the polarization of one photon path, allowing for the observation of both distinguishable and indistinguishable interference patterns.

Considering the low multi-photon contribution of the single-photon signal, the interferometer's contrast, and the intensity difference between the arms, the corrected HOM visibility V_{HOM} is given by [16]

$$V_{\text{HOM}} = \frac{1 + 2g^{(2)}(0)}{2RT(1 - \epsilon)^2} V_{\text{raw}}$$

Here, $V_{\text{raw}} = 1 - \frac{A_{\parallel}}{A_{\perp}}$, with A_{\parallel} and A_{\perp} representing the peak areas at zero delay in the interference patterns for parallel and orthogonal polarizations, respectively. The term $1 - \epsilon$, approximately 0.98, represents the contrast of the interferometer, indicating the spatial overlap of the two photons at the beam splitter. R and T correspond to the reflectance and transmittance of the beam splitter, with values of $R:T \sim 48:52$. $g^{(2)}(0)$ is the measured second-order correlation function value for the single photons.

APPENDIX C: CALIBRATION OF EXTRACTION EFFICIENCY

Table 1 details the various losses in our experimental setup, highlighting an optical system loss of 45.19%. To assess the fiber coupling efficiency, we initially captured the fluorescence emitted by the QD (X^+) using an EMCCD camera. Subsequently, a continuous laser resonant with the QD transition was coupled into the collection fiber, enabling us to visualize its overlap with the QD on the sample. This process determined the single-mode fiber coupling efficiency to be 86.45%. For QD B, as detailed in the main text, the saturation count rate of resonant fluorescence under a " π -pulse" condition, measured by the APD, was 6.23 Mcps. With a detection efficiency of 0.3 and a correction factor of 1.21, and considering the effects of imperfect blinking and losses from optical

Table 1. Efficiency of the Setup^a

Fiber-to-Fiber Efficiency (to APD)	Reflecting Mirror	Objective Lens	Optical Window	APD Efficiency	Free-Space-to-Fiber Efficiency	Blinking (QE)
0.7809	0.8280	0.7597	0.92	0.3 ($\times 1.21$)	0.8645	0.9239

^aThe first four terms represent optical system losses.

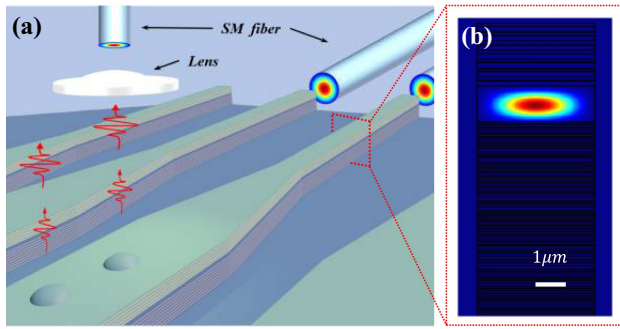


Fig. 7. Waveguide-cavity scheme. (a) Schematic representation of the waveguide-cavity scheme, engineered for spatially orthogonal resonant excitation, showcasing the integration of a QD within a hybrid Fabry-Perot (FP) microcavity-waveguide structure to enhance excitation and photon collection efficiency. (b) Calculated transmission mode profile within the waveguide.

windows and mirrors, the final extraction efficiency was calculated to be approximately 87%.

APPENDIX D: WAVEGUIDE-CAVITY SCHEME

The schematic of the waveguide-cavity scheme and the calculated transmission mode profile within the waveguide are shown in Fig. 7.

Funding. Key R&D Program of Guangdong Province (2020B0303020001); National Natural Science Foundation of China (12074442); Innovation Program for Quantum Science and Technology (2021ZD0301400); Science and Technology Program of Guangzhou (202103030001).

Disclosures. The authors declare no conflicts of interest.

Data Availability. Data underlying the results presented in this paper are not publicly available at this time but may be obtained from the authors upon reasonable request.

REFERENCES

- C. Santori, D. Fattal, J. Vučković, *et al.*, "Indistinguishable photons from a single-photon device," *Nature* **419**, 594–597 (2002).
- P. Michler, A. Kiraz, C. Becher, *et al.*, "A quantum dot single-photon turnstile device," *Science* **290**, 2282–2285 (2000).
- P. Senellart, G. Solomon, and A. White, "High-performance semiconductor quantum-dot single-photon sources," *Nat. Nanotechnol.* **12**, 1026–1039 (2017).
- A. Dousse, J. Suffczyński, A. Beveratos, *et al.*, "Ultrabright source of entangled photon pairs," *Nature* **466**, 217–220 (2010).
- J. Liu, R. Su, Y. Wei, *et al.*, "A solid-state source of strongly entangled photon pairs with high brightness and indistinguishability," *Nat. Nanotechnol.* **14**, 586–593 (2019).
- N. Akopian, N. H. Lindner, E. Poem, *et al.*, "Entangled photon pairs from semiconductor quantum dots," *Phys. Rev. Lett.* **96**, 130501 (2006).
- N. H. Lindner and T. Rudolph, "Proposal for pulsed on-demand sources of photonic cluster state strings," *Phys. Rev. Lett.* **103**, 113602 (2009).
- N. Coste, D. A. Fioretto, N. Belabas, *et al.*, "High-rate entanglement between a semiconductor spin and indistinguishable photons," *Nat. Photonics* **17**, 582–587 (2023).
- D. Cogan, Z. E. Su, O. Kenneth, *et al.*, "Deterministic generation of indistinguishable photons in a cluster state," *Nat. Photonics* **17**, 324–329 (2023).
- Y. M. He, Y. He, Y. J. Wei, *et al.*, "On-demand semiconductor single-photon source with near-unity indistinguishability," *Nat. Nanotechnol.* **8**, 213–217 (2013).
- J.-M. Gerard and B. Gayral, "Strong Purcell effect for InAs quantum boxes in three-dimensional solid-state microcavities," *J. Lightwave Technol.* **17**, 2089–2095 (1999).
- A. Muller, E. B. Flagg, M. Metcalfe, *et al.*, "Coupling an epitaxial quantum dot to a fiber-based external-mirror microcavity," *Appl. Phys. Lett.* **95**, 173101 (2009).
- S. Ates, L. Sapienza, M. Davanco, *et al.*, "Bright single-photon emission from a quantum dot in a circular Bragg grating microcavity," *IEEE J. Sel. Top. Quantum Electron.* **18**, 1711–1721 (2012).
- M. Arcari, I. Söllner, A. Javadi, *et al.*, "Near-unity coupling efficiency of a quantum emitter to a photonic crystal waveguide," *Phys. Rev. Lett.* **113**, 093603 (2014).
- N. Somaschi, V. Giesz, L. De Santis, *et al.*, "Near-optimal single-photon sources in the solid state," *Nat. Photonics* **10**, 340–345 (2016).
- N. Tomm, A. Javadi, N. O. Antoniadis, *et al.*, "A bright and fast source of coherent single photons," *Nat. Nanotechnol.* **16**, 399–403 (2021).
- X. Ding, Y. He, Z. C. Duan, *et al.*, "On-demand single photons with high extraction efficiency and near-unity indistinguishability from a resonantly driven quantum dot in a micropillar," *Phys. Rev. Lett.* **116**, 020401 (2016).
- H. Wang, Y. M. He, T. H. Chung, *et al.*, "Towards optimal single-photon sources from polarized microcavities," *Nat. Photonics* **13**, 770–775 (2019).
- R. Uppu, F. T. Pedersen, Y. Wang, *et al.*, "Scalable integrated single-photon source," *Sci. Adv.* **6**, eabc8268 (2020).
- X. Ding, Y.-P. Guo, M.-C. Xu, *et al.*, "High-efficiency single-photon source above the loss-tolerant threshold for efficient linear optical quantum computing," *arXiv*, arXiv:2311.08347 (2023).
- F. Liu, A. J. Brash, J. O'Hara, *et al.*, "High Purcell factor generation of indistinguishable on-chip single photons," *Nat. Nanotechnol.* **13**, 835–840 (2018).
- A. Muller, E. B. Flagg, P. Bianucci, *et al.*, "Resonance fluorescence from a coherently driven semiconductor quantum dot in a cavity," *Phys. Rev. Lett.* **99**, 187402 (2007).
- Ł. Dusanowski, S. H. Kwon, C. Schneider, *et al.*, "Near-unity indistinguishability single photon source for large-scale integrated quantum optics," *Phys. Rev. Lett.* **122**, 173602 (2019).
- S. Kalliakos, Y. Brody, A. J. Bennett, *et al.*, "Enhanced indistinguishability of in-plane single photons by resonance fluorescence on an integrated quantum dot," *Appl. Phys. Lett.* **109**, 151112 (2016).
- S. Ates, S. M. Ulrich, S. Reitzenstein, *et al.*, "Post-selected indistinguishable photons from the resonance fluorescence of a single quantum dot in a microcavity," *Phys. Rev. Lett.* **103**, 167402 (2009).
- C. Hopfmann, A. Carmele, A. Musiał, *et al.*, "Transition from Jaynes-Cummings to Autler-Townes ladder in a quantum dot-microcavity system," *Phys. Rev. B* **95**, 035302 (2017).
- T. Huber, M. Davanco, M. Müller, *et al.*, "Filter-free single-photon quantum dot resonance fluorescence in an integrated cavity-waveguide device," *Optica* **7**, 380–385 (2020).
- F. Ding, T. Stöferle, L. Mai, *et al.*, "Vertical microcavities with high Q and strong lateral mode confinement," *Phys. Rev. B* **87**, 161116 (2013).
- L. Engel, S. Kolatschek, T. Herzog, *et al.*, "Purcell enhanced single-photon emission from a quantum dot coupled to a truncated Gaussian microcavity," *Appl. Phys. Lett.* **122**, 043503 (2023).
- J. Yang, Y. Chen, Z. Rao, *et al.*, "Tunable quantum dots in monolithic Fabry-Perot microcavities for high-performance single-photon sources," *Light Sci. Appl.* **13**, 33 (2024).
- S. Liu, K. Srinivasan, and J. Liu, "Nanoscale positioning approaches for integrating single solid-state quantum emitters with photonic nanostructures," *Laser Photon. Rev.* **15**, 2100223 (2021).

32. C. H. Bennett and G. Brassard, "Quantum cryptography: public key distribution and coin tossing," *Theor. Comput. Sci.* **560**, 7–11 (2014).
33. S. Aaronson and A. Arkhipov, "The computational complexity of linear optics," in *43rd Annual ACM Symposium on Theory of Computing* (2011), pp. 333–342.
34. N. Tomm, A. R. Korsch, A. Javadi, *et al.*, "Tuning the mode splitting of a semiconductor microcavity with uniaxial stress," *Phys. Rev. Appl.* **15**, 054601 (2021).
35. S. M. Ulrich, S. Ates, S. Reitzenstein, *et al.*, "Dephasing of triplet-sideband optical emission of a resonantly driven InAs/GaAs quantum dot inside a microcavity," *Phys. Rev. Lett.* **106**, 247402 (2011).
36. H. Snijders, J. A. Frey, J. Norman, *et al.*, "Fiber-coupled cavity-QED source of identical single photons," *Phys. Rev. Appl.* **9**, 031002 (2018).
37. J. Goyvaerts, A. Grabowski, J. Gustavsson, *et al.*, "Enabling VCSEL-on-silicon nitride photonic integrated circuits with micro-transfer-printing," *Optica* **8**, 1573–1580 (2021).
38. X. Huang, J. Yang, C. Song, *et al.*, "Self-assembled InAs/GaAs single quantum dots with suppressed InGaAs wetting layer states and low excitonic fine structure splitting for quantum memory," *Nanophotonics* **11**, 3093–3100 (2022).